CrossMark

RESEARCH PAPER

Electroosmotic flow through an α-hemolysin nanopore

Emma Letizia Bonome[1] · Fabio Cecconi[2] · Mauro Chinappi[3,4]

Abstract Nanopores are emerging as powerful tools for biosensing at a single molecule level, and their characterization under different working conditions is crucial for applications. In this perspective, we studied the ionic and electroosmotic flows across an α-hemolysin nanopore using an extensive set of molecular dynamics simulations. Results show that the alteration in the solution pH has a dramatic effect on both electroosmotic flow and nanopore selectivity. Upon lowering the pH, the internal pore surface becomes globally more positively charged and, consequently, the transport of positive ions is hindered leading to a strong unbalance of positive and negative ionic fluxes. This unbalance gives rise to an intense electroosmotic flow that in certain regimes can overwhelm the ionic flux. Finally, we compared our data with continuum prediction for ideal electroosmotic flows, showing that, although the α-hemolysin case is quite far from the ideality, the continuum theory is able to capture the magnitude of the electroosmotic mechanism.

✉ Mauro Chinappi
mauro.chinappi@uniroma2.it

[1] Dipartimento di Ingegneria Meccanica e Aerospaziale, Sapienza Università di Roma, Via Eudossiana 18, 00184 Rome, Italy

[2] CNR-Istituto dei Sistemi Complessi UoS Sapienza, Via dei Taurini 19, 00185 Rome, Italy

[3] Center for Life Nano Science@Sapienza, Istituto Italiano di Tecnologia, Via Regina Elena 291, 00161 Rome, Italy

[4] Dipartimento di Ingegneria Industriale, Università di Roma Tor Vergata, 00133 Rome, Italy

1 Introduction

Electroosmotic flow is the solvent flux induced by an electrostatic force acting on regions of the fluid domain where a net charge is present. The ion distribution nearby a solid-liquid interface is altered by the surface charges resulting in a tiny layer (Debye layer) where a charge unbalance is present (Kirby 2010). An external electrical field tangential to the interface exerts a net force on this layer that, consequently, moves along the wall dragging the bulk of the fluid. Being an interface effect, electroosmotic flow (EOF) is particularly relevant in nanofluidic systems where the surface/volume ratio is large. The interplay between EOF and ion transport has attracted the interest of a varied scientific community with possible applications to particle separation (Malgaretti et al. 2014), enhanced ion transport (Davidson et al. 2016), particle trapping (Asandei et al. 2016; Buyukdagli and Ala-Nissila 2014) and mixing (Belyaev and Vinogradova 2011; Bhattacharyya and Bera 2015).

In this paper, we report results from molecular dynamics simulations of EOF through a α-hemolysin (αHL) channel, a widely employed biological nanopore for single molecule sensing (Wang and Gu 2015; Zhang et al. 2015; Chandramouli et al. 2016; Kasianowicz et al. 2015; Jain et al. 2015; Johnson et al. 2016; Zeng et al. 2015; Stoddart et al. 2015; Breton et al. 2013; Ansalone et al. 2015; Mereuta et al. 2014a, b). The αHL is a 100-Å-long heptameric channel and its interior is constituted by two main regions: the vestibule and the β-barrel, Fig. 1 (Song et al. 1996). The β-barrel, with a cylindrical shape of diameter ~20 Å, is embedded in the lipid membrane. The vestibule stemming from the
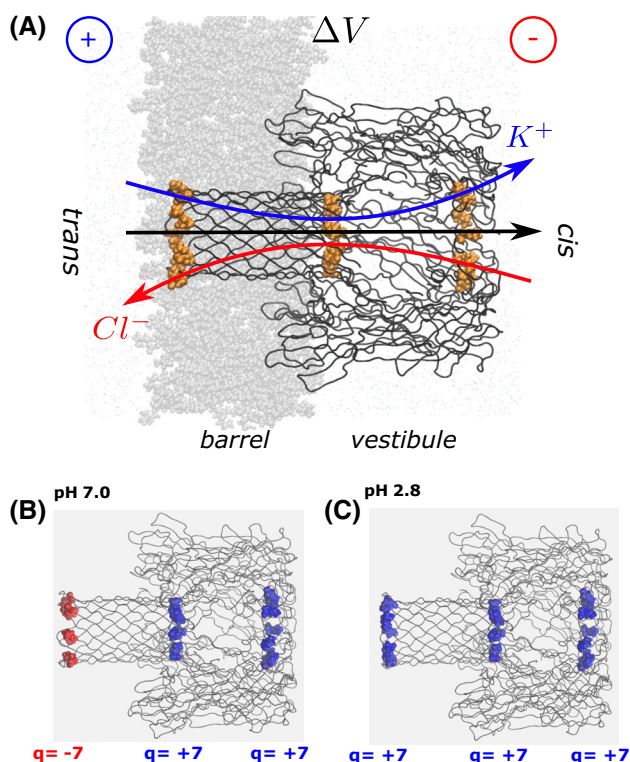
Fig. 1 The α-hemolysin (αHL) nanopore. **a** The pore is embedded in a lipid bilayer (*gray*). The voltage $\Delta V = V_{cis} - V_{trans}$ is applied between the *cis* and *trans* compartments. The *black arrow* indicates the total current I (positive from *trans* to *cis*), while the *blue* and *red arrows* indicate the cationic (I^+, positive from *trans* to *cis*) and anionic (I^-, positive from *cis* to *trans*) contributions, respectively. Water, ions and several lipid molecules are not reported for clarity. *Cis* entrance (diameter ~25 Å), constriction (diameter ~14 Å) and trans entrance (diameter ~20 Å) are sketched in *orange*. **b, c** Total charge q of Cis entrance, constriction and trans entrance at pH = 7 and pH = 2.8. Positively (negatively) charged amino acids for these three regions are shown in *blue* (*red*). Figures S2 and S3 of the supporting information report the complete list of protonated residues and the electrical potential along the pore axis calculated for both pHs (color figure online)

membrane is wider than the β-barrel and its maximum diameter is ~46 Å. These two regions are connected by a constriction that constitutes the pore narrowest section of diameter ~14 Å. The positively charged constriction is responsible for the αHL ion selectivity, a property that has already been the subject of numerical (Aksimentiev and Schulten 2005; Bhattacharya et al. 2011) and experimental investigations (Merzlyak et al. 2005; Piguet et al. 2014) at different salt compositions. Recent experimental studies by Piguet et al. (2014), Asandei et al. (2016) and Boukhet et al. (2016) interpreted the voltage dependency of capture and residence time of macromolecules as an effect of EOF across the αHL.

Several charged residues, exposed toward the interior of the pore, strongly affect both ionic and electroosmotic flows. The charge of such residues can be altered by varying the pH of the solution. In particular, the pore interior becomes more and more positively charged upon lowering the pH, as aspartic acid and glutamic acid can be neutralized, whereas histidine, lysine and arginine can acquire a positive charge. The interested reader can find a complete description of the αHL pore and of the exposed charged residues in the above-cited literature. For the aim of this paper, we mainly need to focus on three specific regions of the pore, namely the two pore entrances (*trans* and *cis*) and the constriction. The net charge of such regions at different pH is reported in Fig. 1b, c

The paper is structured as follows. Section 2 reports the details of the all-atom molecular dynamics setup and describes how the fluxes are extracted from the system trajectories. The results are reported in Sect. 3 along with a comparison with existing quantitative theories.

2 Methods

The initial conformation of the system was assembled by using standard protocols described in Aksimentiev and Schulten (2005), Comer et al. (2011), Di Marino et al. (2015) and briefly summarized below. We started from the αHL crystal structure pdb_id: 7AHL (Song et al. 1996) downloaded from the OPM database (Lomize et al. 2006). The membrane, the water molecules and the ions were added using VMD (Humphrey et al. 1996). Then, the system was minimized and a 60 ps NVT simulation (time step 0.2 fs) was run. Following Comer et al. (2011), during this stage, external forces are added to avoid water molecules entering the membrane, while αHL and lipid heads were constrained. A further 1 ns NPT flexible cell simulation [time step 1 fs, Nosé–Hoover–Langevin piston Martyna et al. (1994)] was employed to compact the membrane. During this run, the lipid molecules were let free to move. The third, and last, equilibration stage consists in a 2 ns NPT constant area simulations (time step 2 fs) where all the atoms are unconstrained. The resulting periodic box after the equilibration has the following dimensions $L_x = 126.49$ Å, $L_y = 124.61$ Å and $L_z = 217.5$ Å and the number of atoms is ~370,000. A complete description of the system is reported in Figure S1 of the supporting information.

The equilibrated configuration was used for non-equilibrium runs at different voltages. A uniform and constant external electric field $\mathbf{E} = (0, 0, E_z)$ was applied perpendicularly to the lipid bilayer. This protocol was shown to be equivalent to the application of a constant voltage $\Delta V = E_z L_z$ (Gumbart et al. 2012). The resulting applied electrical field is in the range $0.5 \div 0.05 \times 10^8$ V/m that is below the threshold for affecting both apparent permittivity and dipole moment profile (Marracino et al. 2015). Each simulation was run for 70 ns and

snapshots are saved every $\Delta t = 40$ ps. The average current in the interval $[t, t + \Delta t]$ is estimated as

$$I(t) = \frac{1}{\Delta t \, L_z} \sum_{i=1}^{N} q_i [z_i(t + \Delta t) - z_i(t)] \qquad (1)$$

where q_i and z_i are charge and the z-coordinate of the ith atom, respectively. The K^+ and Cl^- currents were computed by restricting the sum over the atoms of corresponding type (Aksimentiev and Schulten 2005). The mean current is obtained via a time average of $I(t)$ after discarding a transient of 1 ns. Errors are estimated using block average protocols (Allen and Tildesley 1989). The sum in Eq. (1) with $q_i = 1$, when restricted to the water molecules, provides the EOF.

The same setup was used for both pH = 7 and pH = 2.8, the only difference being the protonation state of some specific residues. For pH = 7, we assigned the residues the standard protonation states, while for pH = 2.8 we employed the H++ server version 3.2 (Anandakrishnan et al. 2012) to determine the protonation degree of titratable residues. The server provided a pK_a value for each single amino acid in each different αHL chain. We protonated all the residues for which the pK_a averaged over the seven chains is larger than 2.8, by using psfgen tools included in VMD (Humphrey et al. 1996). The methodology and the list of the protonated residues are reported in the supporting information (Section S1; Figure S2).

All MD simulations were performed using NAMD software (Phillips et al. 2005) by implementing periodic boundary conditions and particle mesh Ewalds (PME) summation method for the electrostatics (Batcho et al. 2001). The CHARMM36 force field (Brooks et al. 2009; Vanommeslaeghe and MacKerell 2012) was employed to model lipid, protein and TIP3P water molecules (Jorgensen et al. 1983). NBFIX corrections were applied for ions (Luo and Roux 2009).

3 Results

The system setup is reported in Fig. 1a. An applied electrical field acts normally to the membrane. We conventionally define the *cis* side as ground ($V = 0$) so that a positive (negative) ΔV corresponds to *trans→cis*(*cis→ trans*) current. Here we report data for 2M KCl concentrations, while the results for 1M KCl are discussed in the supporting information.

3.1 Current–voltage characteristic

The resulting total ionic current $I = I^+ + I^-$ as function of the voltage ΔV is shown in Fig. 2a, while the cationic

I^+ and anionic I^- contributions are reported in Fig. 2b, c, respectively.

pH = 7. For low voltages, $|\Delta V| < 0.2V$, the total ionic current I is linear in ΔV (Ohmic regime). The resulting αHL ionic conductance is $G = I/\Delta V = 1.96 \pm 0.28$ nS in quite good agreement with experimental results, such as Rodriguez-Larrea and Bayley (2013) ($G = 2.07$ nS at $\Delta V = 0.14$ V), Mereuta et al. (2014b) ($G = 1.63$ nS at $\Delta V = 0.05$ V) and Campos et al. (2012) ($G = 2.18$ nS at $\Delta V = 0.08$ V).

At high voltages, the $I - V$ curve presents an asymmetry characterized by a larger current intensity at positive ΔV, Fig. 2a. The same happens also to anionic and cation contributions, Fig. 2b, c. This behavior can be easily explained by considering the field generated by those charges localized at the two ends of αHL pore. At negative ΔV, the anions Cl^- enter from the trans side (red arrow in Fig. 2d). The presence of the electrostatic repulsion, caused by the negative charges at the barrel entrance, hinders the anionic flux into the pore. Conversely, for $\Delta V > 0$, the anions enter the cis side. In this case, the presence of a positive charge at the vestibule entrance attracts the Cl^- ions increasing their flow into to nanopore. The same argument applies to the cationic (K^+) current: At negative ΔV, the cations K^+ enter the cis side (blue arrow in Fig. 2d) where they found a repelling pore charge that reduces the current. Instead, for positive ΔV, the cations enter the trans side and are attracted by the negative charges at the barrel entrance. Hence, also the cationic current is asymmetric and it is larger at $\Delta V > 0$.

pH = 2.8. In this case, the $I - V$ curves are quite symmetric with respect to the origin (2a, solid line). The low pH affects the protonation states of several exposed residues and, in particular, even the trans entrance turns to be positively charged, Fig 2e. The comparison between the electrostatic potential along the pore axis generated by the αHL at the two selected pH is reported in Figure S3. It is apparent that that pH = 2.8 the electrostatic potential is always positive inside the pore. Hence, no strong asymmetry is expected in $I - V$ characteristic as both barrel and vestibule ends acquire positive charges. Also in this case, at low voltages, $|\Delta V| < 0.2$ V, the conductance $G = 2.24 \pm 0.13$ ns is consistent with experiments by Campos et al. (2012) $G = 2.1$ ns at $\Delta V = 0.08$ V.

The rectification of the current in the αHL system was investigated by several authors, see, among others (Bhattacharya et al. 2011) for a combined computational and experimental analysis. The $I - V$ asymmetry is not a peculiarity pertaining to biological pores, but it is also observed in solid-state nanopores (Thangaraj et al. 2016; Laohakunakorn et al. 2014), and it even occurs in uncharged channels when interacting to strongly charged molecules (Chinappi et al. 2014).
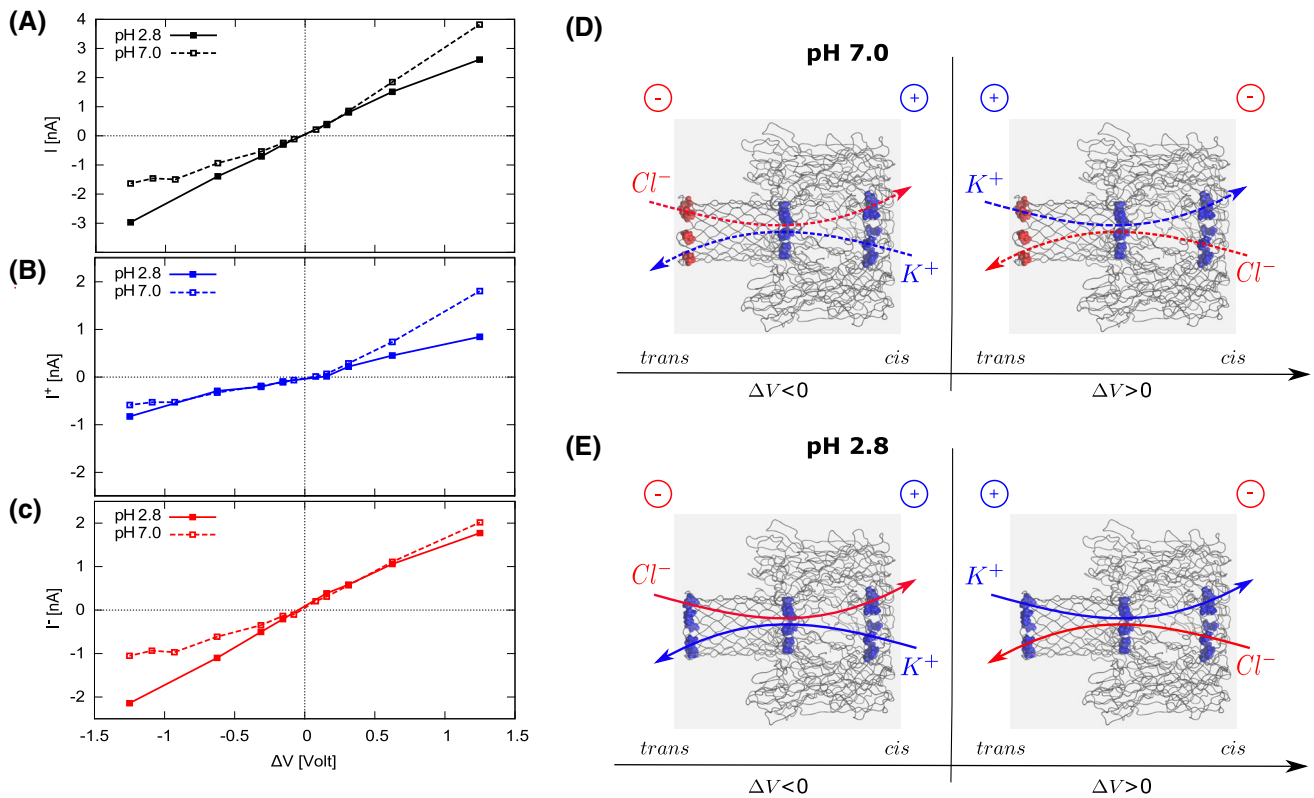
Fig. 2 **a–c** $I - V$ characteristics for 2 M KCl simulations at pH = 2.8 (*solid line*) and $pH = 7.0$ (*dashed line*). Total current I is in *black*, while I^+ and I^- are in *blue* and *red*, respectively. The 1 M KCl case is reported in S4 of the supporting information. **d**, **e** Direction of ionic flows through αHL for positive and negative ΔV. The red and blue arrows represent the direction of anionic and cationic currents at pH = 7.0 (*dashed arrow*, panel **d** and pH = 2.8 (*solid arrow*, panel **e**) (color figure online)

Effect of ionic concentration. Standard continuum approaches suggest, for dilute solution, a ionic conductivity proportional to ionic concentration. Consequently, also the nanopore conductance, G, in the linear regime (low voltage) is expected to be proportional to the ionic concentration. Figure S7 reports G as a function of the ionic concentration, showing that data are compatible with a linear behavior. It is worth noting that this condition is often not fulfilled in nanoscale systems at ionic concentration comparable with the one used in this work. For instance, in Liu et al. (2010), ionic currents through carbon nanotubes do not depend linearly on the ion concentration, an occurrence that the authors imputed to the presence of a very intense electroosmotic flow generated by an excess of charge inside the pore.

3.2 Selectivity

A further consequence of the αHL surface charges is the anionic selectivity. Besides the charges at the two entrances, there is a ring of positively charged residues in the αHL constriction that is also relevant to anionic selectivity as they are located in the narrowest region of the

channel (Kasianowicz et al. 1999; Campos et al. 2012). Figure 4a reports the ratio I^-/I as a function of ΔV for pH = 2.8 and $pH = 7$, solid and dashed lines, respectively. In all the considered cases, the total current is dominated by the anionic flow ($I^-/I > 0.5$). At lower pH, the pore becomes more anionic-selective as expected form the presence of an excess of positive charges on its internal surface. Figure 3 shows the Cl^- and K^+ concentration maps for pH = 7 and pH = 2.8 at $\Delta V = 0$. At lower pH, a strong depletion of K^+ ion is observed in the barrel.

3.3 Electroosmosis

Figure 4b displays the electroosmotic flow (EOF) Φ_{eo} expressed in number of water molecules for ns. The EOF is directed as the negative ions, i.e., it is positive at negative ΔV. Despite large error bars, it is apparent that EOF is present at both pH values and is larger at the smaller one. This is consistent with the increased anionic selectivity observed at pH = 2.8. It is interesting to note that Φ_{eo} is larger than the corresponding ionic flows expressed in number of ion/ns, Φ_{Cl^-} and Φ_{K^+} in the following. For instance, for pH = 2.8 at $\Delta V = -1.25$, $\Phi_{eo} \sim 50 \, \mathrm{ns}^{-1}$,
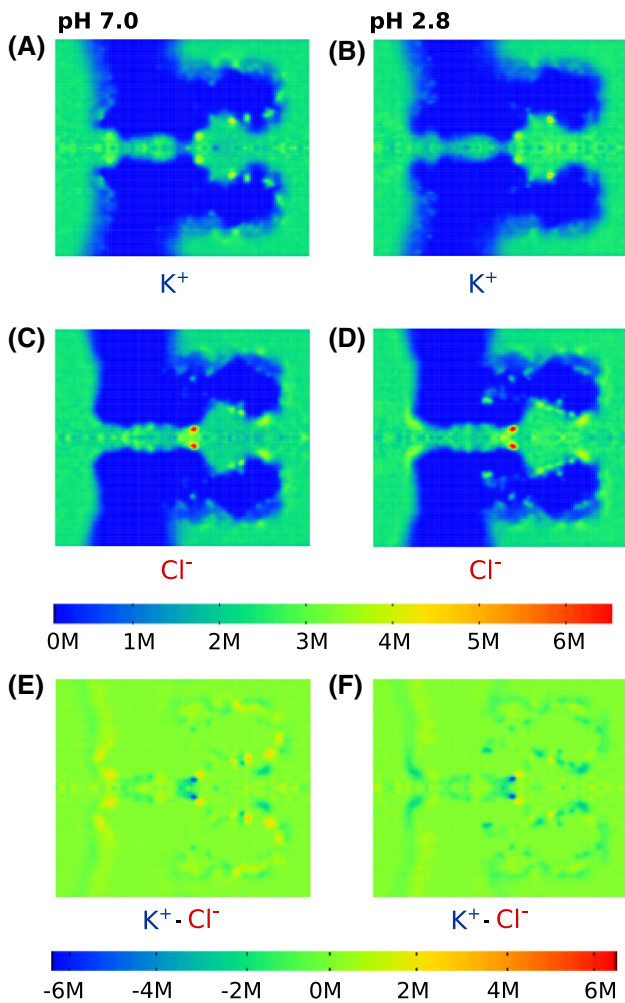
Fig. 3 **a–d** Ion concentration maps for Cl⁻ and K⁺ at $\Delta V = 0$ for 2M KCl. The regions not accessible to ions (membrane and channel) are in *blue*. The *red peaks* at both pH in the Cl⁻ density correspond to the charge accumulation caused by the presence of positive-residue ring at the constriction, panel **c**, **d**. A marked depletion of K⁺ ions in the barrel region for pH = 2.8 indicates the enhancement of the pore selectivity at low *pH*, panel **d**. The distribution of the net charge for pH = 7 and pH = 2.8 is reported in the panel **e**, **f**, respectively. The 1 M KCl case is reported in S6 of the supporting information (color figure online)

while $\Phi_{\text{Cl}^-} = 13.1\,\text{ns}^{-1}$ and $\Phi_{\text{K}^+} = -5.6\,\text{ns}^{-1}$. This can be explained presuming that each ion drags a hydration shell of n_c water molecules with n_c the hydration number that, for Cl⁻ and K⁺, is ∼6 (Mancinelli et al. 2007). The magenta symbols in Fig. 4b correspond to the expression

$$\Phi_{eo} = n_c(\Phi_{\text{Cl}^-} - \Phi_{\text{K}^+}), \tag{2}$$

in a fair agreement with the data. A similar argument was suggested in Piguet et al. (2014) to estimate the electroosmotic flow from experimental data.

In the literature, EOF is commonly described by continuum approaches; hence, it is reasonable to test the reliability of those theories against our numerical results.
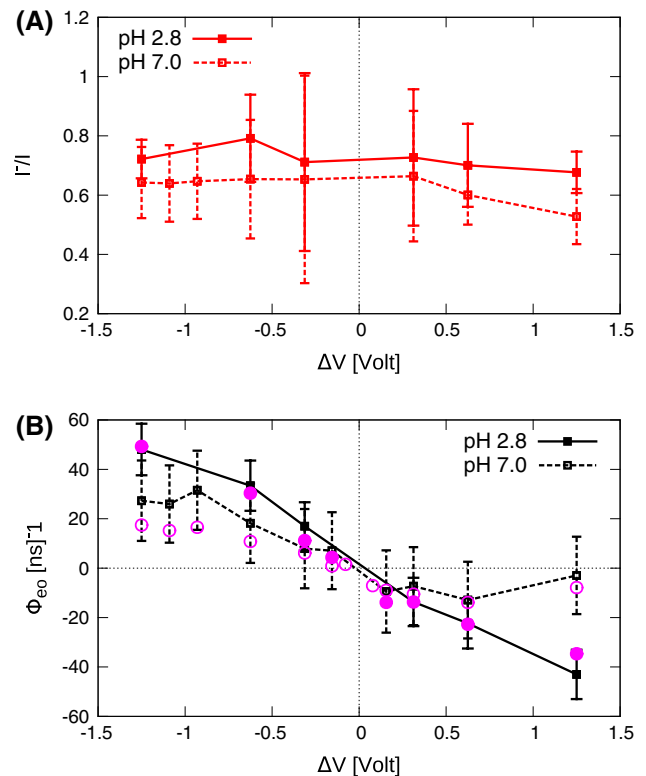

Fig. 4 Ion selectivity and electroosmotic flow. **a** Anionic current fraction I^-/I as a function of ΔV at pH = 2.8 (*solid line*) and pH = 7.0 (*dashed line*) for 2 M KCl. In both cases, the average values are larger than 0.5 indicating that the current is dominated by negative carriers. Data at low voltages are not reported since the error bars overwhelm the average values. **b** Electroosmotic flow Φ_{eo} (number of molecules for ns) as a function of ΔV. The *circles* in *magenta* (open pH = 7, filled pH = 2.8), correspond to the estimation provided by Eq. (2). The 1 M KCl case is reported in Figure S5 of supporting information (color figure online)

As a first model, we can estimate Φ_{eo} using the ideal electroosmotic flow formulation for a cylinder of radius a and length L, for $L \gg a$. We report here the main steps; the interested reader can find a detailed derivation, among others, in Bruus (2008). The cylinder surface is assumed to be uniformly charged with density σ corresponding to a ζ-potential

$$\zeta = \frac{\sigma \lambda_D}{\epsilon_0 \epsilon_r} \tag{3}$$

with

$$\lambda_D = \sqrt{\frac{\epsilon_0 \epsilon_r k_B T}{2(Ze)^2 c_o}} \tag{4}$$

the Debye length, e the electron charge, Z the ion valence, c_0 the ionic bulk concentration, k_B the Boltzmann constant, T the temperature and ϵ_0 and ϵ_r the vacuum and

relative permittivities. Under the action of a homogeneous and constant electrical field $E = \Delta V/L$, the velocity along the cylinder axis is

$$v(r) = v_{eo} \left[1 - \frac{I_0\left(\frac{r}{\lambda_D}\right)}{I_0\left(\frac{a}{\lambda_D}\right)} \right] \tag{5}$$

where

$$v_{eo} = \frac{\epsilon_0 \epsilon_r \zeta E}{\mu} = \frac{\sigma \lambda_D \Delta V}{\mu L} \tag{6}$$

with μ being the viscosity and I_0 the zero-order modified Bessel function of first kind. Integrating $v(r)$ over the cylinder section, the flow rate Φ_{eo} is easily obtained as

$$\Phi_{eo} = G_{eo} \Delta V \tag{7}$$

with

$$G_{eo} = 2\pi \frac{\sigma \lambda_D}{\mu L} \int_0^a r \left[1 - \frac{I_0\left(\frac{r}{\lambda_D}\right)}{I_0\left(\frac{a}{\lambda_D}\right)} \right] dr. \tag{8}$$

In analogy with the electric conductance G, we indicate the quantity G_{eo} as electroosmotic conductance, i.e., the electroosmotic flow Φ_{eo} per unit of voltage. Equation (8) involves a large number of effective parameters for which reasonable estimations have to be provided; otherwise, the results will arbitrarily depend on the selected values. Here, we chose $a = 7$ Å and $L = 100$ Å for the pore size, $\eta = 3.1 \cdot 10^{-4}$ Kg/ms for the TIP3P water viscosity (González and Abascal 2010), $\sigma = q_s/(2\pi a L)$ for the surface charge, where q_s is the total charge of the residues exposed to the pore interior. For pH = 2.8, a reasonable value for the surface charge is $q_s = 14e$ (see Supporting Information) with e the electron charge. This leads to particle flow rate of $G_{eo} \simeq 90$ (ns V)$^{-1}$. Surprisingly, this very crude approximation is able to catch the order of magnitude of the simulated EOF.

A second estimation for Φ_{eo} can be achieved from Hagen–Poiseuille expression for the flow rate in a cylindrical channel under the action of a homogeneous and constant volume force g that can be easily obtained integrating the parabolic velocity profile leading to

$$\Phi_{eo} = \frac{\pi a^4}{8\mu} g. \tag{9}$$

The positive surface charge q_s induces an excess of negative ion density $q_s/(\pi a^2 L)$ inside the pore to reach a global electroneutrality, resulting in an average net force

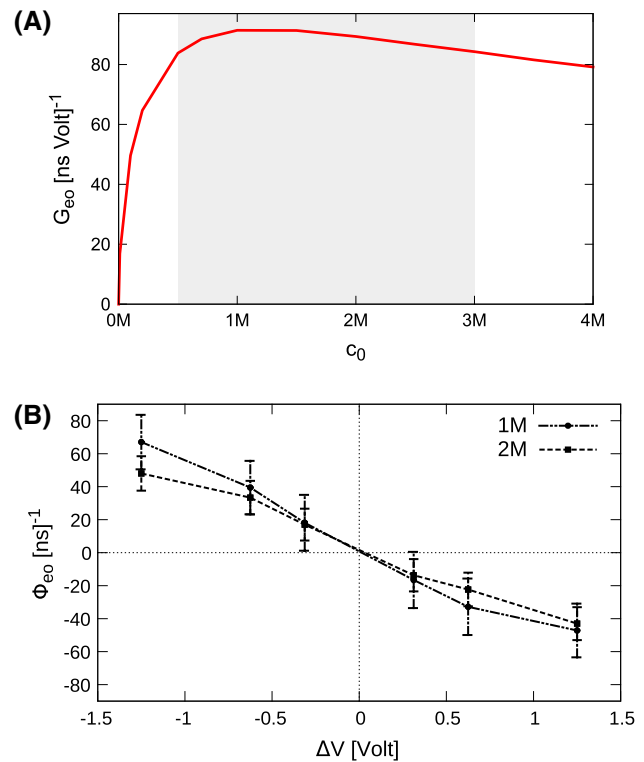$$g = \frac{q_s}{\pi a^2 L} \frac{\Delta V}{L} \tag{10}$$

Fig. 5 **a** Theoretical estimation of G_{eo} by ideal electroosmotic flow, Eq. (8), as a function of the bulk ionic concentration c_0. The *shaded region* indicates the range $c_0 \in (0.5, 3 \text{ M})$ that is the relevant one to nanopore sensing. It is apparent that G_{eo} is almost constant in this interval. Panel **b** reports the electroosmotic flow Φ_{eo} for pH = 2.8 at different molarities (1 and 2 M) measured by molecular dynamics simulations

leading to an electroosmotic conductance

$$G_{eo} = \frac{a^2}{8\mu} \frac{q_s}{L^2}. \tag{11}$$

Using the same parameters as before, we find a particle flow of $G_{eo} \simeq 152(\text{nsV})^{-1}$, that, again, is of the same order of magnitude of the simulation results.

The expressions for electroosmotic conductance (8) and (11) allow to understand, at least qualitatively, the effect of the various parameters. For instance, it is obvious that, in both formulas, G_{eo} linearly depends on the surface charge σ and, hence, on the exposed charge inside the pore. This explains why the electroosmotic flow turns to be smaller at the highest pH= 7.

An interesting point, emerging from both expressions, is the weak influence of the bulk ionic concentration c_0 on G_{eo}. Equation (11) is independent on c_0, while c_0 enters Eq. (8) via the Debye length λ_D and, consequently, it influences both the prefactor and the integral of expression (8). However, as shown in Fig. 5a, the combination of the two effects brings to an almost flat G_{eo} behavior, at least in the range between 0.5 and 3M that is relevant to nanopore

sensing. Figure 5b reports EOF for 1 and 2 M at pH = 2.8. It is apparent that, as indicated by both theoretical models, the EOF does not appreciably change with the bulk ion concentration.

The simplified theories we discussed do not take into account the liquid slippage at solid-liquid interface. Although slippage can strongly affect the flow at nanoscale (Bakli and Chakraborty 2016; Chinappi and Casciola 2010), we expect that, for a rough interface like the αHL interior, the no-slip condition remains a reasonable approximation. Another effect that can be potentially included in the continuum models is the increase in the effective viscosity due the adsorption of ions on the pore surface, as discussed in Knecht et al. (2013) and Qiao and Aluru (2003). The viscosity increase can partially explain the overestimation of the EOF prediction resulting by the continuum theories we employed. Another limitation of results (8) and (11) stems form the ion finite-size effect that, at high concentration, can have a significant impact on charge distribution and, consequently, on EOF. Several modifications of the classical point-charge Poisson–Boltzmann (PB) equation have been proposed in the literature (Qiao and Aluru 2003; Paunov and Binks 1999; Borukhov et al. 2000). The works Paunov and Binks (1999) and Borukhov et al. (2000) that explicitly took into account ion finite-size effects obtained a saturated counterion concentration very near to a charged surface that is lower than the PB prediction. However, farther from the surface, they found counterion concentrations that are systematically larger than that expected by a point-charge approach. The ambiguity due to overestimation and underestimation of concentrations makes it difficult to assess whether, in our case, the inclusion of the finite-size effects is able to improve the theoretical estimation of the EOF.

4 Conclusions

We simulated via all-atom molecular dynamics the ionic and electroosmotic flow across an α-hemolysin nanopore under the action of an applied voltage. Our data show that the pH decrease, inducing a protonation of exposed residues, has a relevant effect on both ionic and electroosmotic flows. Specifically, the ionic flow is characterized by a pronounced anionic selectivity of the pore, while the electroosmotic flow increases at low pH.

We found that the electroosmotic flow is associated with the unbalance between positive and negative ionic fluxes and it turns to be strong enough to overwhelm the ionic current, i.e., the number of water molecules streaming through the pore per unit of time is larger than the number of flowing ions. A surprising simple argument, based on ionic hydration number, is able to link the electroosmotic flow to the anionic and cation currents.

Our data support and complement the experimental observation by Piguet et al. (2014) and Asandei et al. (2016) where the electroosmosis was not directly measured, but was invoked to explain alteration of ion current due to macromolecule interaction with a nanopore.

Finally, we tested the reliability of two simple continuum models for ideal electroosmosis, showing that they are able to catch the order of magnitude of the electroosmotic flow even in conditions far from ideality, as in the case of narrow and complex channels like α-hemolysin.

References

Aksimentiev A, Schulten K (2005) Imaging α-hemolysin with molecular dynamics: ionic conductance, osmotic permeability, and the electrostatic potential map. Biophys J 88(6):3745–3761

Allen MP, Tildesley DJ (1989) Computer simulation of liquids. Oxford University Press, Oxford

Anandakrishnan R, Aguilar B, Onufriev AV (2012) H++ 3.0: automating pk prediction and the preparation of biomolecular structures for atomistic molecular modeling and simulations. Nucl Acids Res 40(W1):W537–W541

Ansalone P, Chinappi M, Rondoni L, Cecconi F (2015) Driven diffusion against electrostatic or effective energy barrier across α-hemolysin. J Chem Phys 143(15):154,109

Asandei A, Schiopu I, Chinappi M, Seo CH, Park Y, Luchian T (2016) Electroosmotic trap against the electrophoretic force near a protein nanopore reveals peptide dynamics during capture and translocation. ACS Appl Mater Interfaces 8(20):166–179

Bakli C, Chakraborty S (2016) Rapid capillary filling via ion-water interactions over the nanoscale. Nanoscale 8(12):6535–6541

Batcho PF, Case DA, Schlick T (2001) Optimized particle-mesh Ewald/multiple-time step integration for molecular dynamics simulations. J Chem Phys 115(9):4003–4018

Belyaev AV, Vinogradova OI (2011) Electro-osmosis on anisotropic superhydrophobic surfaces. Phys Rev Lett 107(9):098,301

Bhattacharyya S, Bera S (2015) Combined electroosmosis-pressure driven flow and mixing in a microchannel with surface heterogeneity. Appl Math Model 39(15):4337–4350

Bhattacharya S, Muzard J, Payet L, Mathé J, Bockelmann U, Aksimentiev A, Viasnoff V (2011) Rectification of the current in α-hemolysin pore depends on the cation type: the alkali series probed by molecular dynamics simulations and experiments. J Phys Chem C 115(10):4255–4264

Borukhov I, Andelman D, Orland H (2000) Adsorption of large ions from an electrolyte solution: a modified poisson-boltzmann equation. Electrochim Acta 46(2):221–229

Boukhet M, Piguet F, Ouldali H, Pastoriza-Gallego M, Pelta J, Oukhaled A (2016) Probing driving forces in aerolysin and α-hemolysin biological nanopores: electrophoresis versus electroosmosis. Nanoscale 8(43):18,352–18,359

Breton MF, Discala F, Bacri L, Foster D, Pelta J, Oukhaled A (2013) Exploration of neutral versus polyelectrolyte behavior of poly (ethylene glycol) s in alkali ion solutions using single-nanopore recording. J Phys Chem Lett 4(13):2202–2208

Brooks BR, Brooks CL, MacKerell AD, Nilsson L, Petrella RJ, Roux B, Won Y, Archontis G, Bartels C, Boresch S et al (2009) Charmm: the biomolecular simulation program. J Comput Chem 30(10):1545–1614

Bruus H (2007) Theoretical microfluidics. Oxford University Press, Oxford

Buyukdagli S, Ala-Nissila T (2014) Controlling polymer translocation and ion transport via charge correlations. Langmuir 30(43):12,907–12,915

Campos E, Asandei A, McVey CE, Dias JC, Oliveira ASF, Soares CM, Luchian T, Astier Y (2012) The role of lys147 in the interaction between mpsa-gold nanoparticles and the α-hemolysin nanopore. Langmuir 28(44):15,643–15,650

Chandramouli B, Di Maio D, Mancini G, Brancato G (2016) Introducing an artificial photo-switch into a biological pore: A model study of an engineered α-hemolysin. Biochim Biophys Acta Biomembr 1858(4):689–697

Chinappi M, Casciola C (2010) Intrinsic slip on hydrophobic self-assembled monolayer coatings. Phys Fluids 22(042):003

Chinappi M, Casciola CM, Cecconi F, Marconi UMB, Melchionna S (2014) Modulation of current through a nanopore induced by a charged globule: implications for dna-docking. Europhys Lett 108(4):46,002

Comer JR, Wells DB, Aksimentiev A (2011) Modeling nanopores for sequencing DNA. Methods Mol Biol 749:317–358. doi:10.1007/978-1-61779-142-0_22

Davidson SM, Wessling M, Mani A (2016) On the dynamical regimes of pattern-accelerated electroconvection. Sci rep 6:22505

Di Marino D, Bonome EL, Tramontano A, Chinappi M (2015) All-atom molecular dynamics simulation of protein translocation through an α-hemolysin nanopore. J Phys Chem Lett 6(15):2963–2968

González MA, Abascal JL (2010) The shear viscosity of rigid water models. J Chem Phys 132(9):096,101

Gumbart J, Khalili-Araghi F, Sotomayor M, Roux B (2012) Constant electric field simulations of the membrane potential illustrated with simple systems. Biochim Biophys Acta Biomembr 1818(2):294–302

Humphrey W, Dalke A, Schulten K (1996) Vmd: visual molecular dynamics. J Mol Graph 14(1):33–38

Jain M, Fiddes IT, Miga KH, Olsen HE, Paten B, Akeson M (2015) Improved data analysis for the minion nanopore sequencer. Nat Methods 12(4):351–356

Johnson RP, Fleming AM, Beuth LR, Burrows CJ, White HS (2016) Base flipping within the α-hemolysin latch allows single-molecule identification of mismatches in DNA. J Am Chem Soc 138(2):594–603. doi:10.1021/jacs.5b10710

Jorgensen WL, Chandrasekhar J, Madura JD, Impey RW, Klein ML (1983) Comparison of simple potential functions for simulating liquid water. J Chem Phys 79(2):926–935

Kasianowicz JJ, Burden DL, Han LC, Cheley S, Bayley H (1999) Genetically engineered metal ion binding sites on the outside of a channel's transmembrane β-barrel. Biophys J 76(2):837–845

Kasianowicz JJ, Balijepalli AK, Ettedgui J, Forstater JH, Wang H, Zhang H, Robertson JW (2016) Analytical applications for pore-forming proteins. Biochim Biophys Acta Biomembr 1858(3):593–606

Kirby BJ (2010) Micro-and nanoscale fluid mechanics: transport in microfluidic devices. Cambridge University Press, Cambridge

Knecht V, Klasczyk B, Dimova R (2013) Macro-versus microscopic view on the electrokinetics of a water-membrane interface. Langmuir 29(25):7939–7948

Laohakunakorn N, Thacker VV, Muthukumar M, Keyser UF (2014) Electroosmotic flow reversal outside glass nanopores. Nano Lett 15(1):695–702

Liu H, He J, Tang J, Liu H, Pang P, Cao D, Krstic P, Joseph S, Lindsay S, Nuckolls C (2010) Translocation of single-stranded dna through single-walled carbon nanotubes. Science 327(5961):64–67

Lomize MA, Lomize AL, Pogozheva ID, Mosberg HI (2006) Opm: orientations of proteins in membranes database. Bioinformatics 22(5):623–625

Luo Y, Roux B (2009) Simulation of osmotic pressure in concentrated aqueous salt solutions. J Phys Chem Lett 1(1):183–189

Malgaretti P, Pagonabarraga I, Rubi JM (2014) Entropic electrokinetics: recirculation, particle separation, and negative mobility. Phys Rev Lett 113(12):128,301

Mancinelli R, Botti A, Bruni F, Ricci M, Soper A (2007) Hydration of sodium, potassium, and chloride ions in solution and the concept of structure maker/breaker. J Phys Chem B 111(48):13,570–13,577

Marracino P, Liberti M, d'Inzeo G, Apollonio F (2015) Water response to intense electric fields: a molecular dynamics study. Bioelectromagnetics 36(5):377–385

Martyna GJ, Tobias DJ, Klein ML (1994) Constant pressure molecular dynamics algorithms. J Chem Phys 101(5):4177–4189

Mereuta L, Asandei A, Seo CH, Park Y, Luchian T (2014a) Quantitative understanding of ph-and salt-mediated conformational folding of histidine-containing, β-hairpin-like peptides, through single-molecule probing with protein nanopores. ACS Appl Mater Interfaces 6(15):13,242–13,256

Mereuta L, Roy M, Asandei A, Lee JK, Park Y, Andricioaei I, Luchian T (2014b) Slowing down single-molecule trafficking through a protein nanopore reveals intermediates for peptide translocation. Sci Rep 4:3885

Merzlyak PG, Capistrano MFP, Valeva A, Kasianowicz JJ, Krasilnikov OV (2005) Conductance and ion selectivity of a mesoscopic protein nanopore probed with cysteine scanning mutagenesis. Biophys J 89(5):3059–3070

Paunov VN, Binks BP (1999) Analytical expression for the electrostatic disjoining pressure taking into account the excluded volume of the hydrated ions between charged interfaces in electrolyte. Langmuir 15(6):2015–2021

Phillips JC, Braun R, Wang W, Gumbart J, Tajkhorshid E, Villa E, Chipot C, Skeel RD, Kale L, Schulten K (2005) Scalable molecular dynamics with namd. J Comput Chem 26(16):1781–1802

Piguet F, Discala F, Breton MF, Pelta J, Bacri L, Oukhaled A (2014) Electroosmosis through α-hemolysin that depends on alkali cation type. J Phys Chem Lett 5(24):4362–4367

Qiao R, Aluru N (2003) Ion concentrations and velocity profiles in nanochannel electroosmotic flows. J Chem Phys 118(10):4692–4701

Rodriguez-Larrea D, Bayley H (2013) Multistep protein unfolding during nanopore translocation. Nat Nanotechnol 8(4):288–295

Song L, Hobaugh MR, Shustak C, Cheley S, Bayley H, Gouaux JE (1996) Structure of staphylococcal α-hemolysin, a heptameric transmembrane pore. Science 274(5294):1859–1865

Stoddart D, Franceschini L, Heron A, Bayley H, Maglia G (2015) Dna stretching and optimization of nucleobase recognition in enzymatic nanopore sequencing. Nanotechnology 26(8):084,002

Thangaraj V, Lepoitevin M, Smietana M, Balanzat E, Bechelany M, Janot JM, Vasseur JJ, Subramanian S, Balme S (2016) Detection of short ssdna and dsdna by current–voltage measurements using conical nanopores coated with al2o3 by atomic layer deposition. Microchim Acta 183(3):1011–1017

Vanommeslaeghe K, MacKerell AD Jr (2012) Automation of the charmm general force field (cgenff) i: bond perception and atom typing. J Chem Inf Model 52(12):3144–3154

Wang Y, Gu LQ (2015) Biomedical diagnosis perspective of epigenetic detections using alpha-hemolysin nanopore. AIMS Mater Science 2(4):448–472

Zeng T, Liu L, Li T, Li Y, Gao J, Zhao Y, Wu HC (2015) Detection of 5-methylcytosine and 5-hydroxymethylcytosine in dna via host-guest interactions inside α-hemolysin nanopores. Chem Sci 6(10):5628–5634

Zhang X, Xu X, Yang Z, Burcke AJ, Gates KS, Chen SJ, Gu LQ (2015) Mimicking ribosomal unfolding of rna pseudoknot in a protein channel. JACS 137(50):15,742–15,752